ACES Asian Chemical Editorial Society

doi.org/10.1002/cnma.202300383

CHEMNANOMAT
Research Article

www.chemnanomat.org

Folic Acid-Modified Nanoprobe for In Vivo-Targeted Persistent Luminescence Imaging and pH-Responsive Antibiotic Therapy of Bacterial Infection

Li-Ya Wang,[a, b, c] Li-Xia Yan,[a, b, c] Xu Zhao,[a, b, c] Li-Jian Chen,[a, b, c] and Xiu-Ping Yan*[a, b, c]

Low antibiotic utilization and inability to achieve real-time monitoring of pathological status and treatment processes often result in unsatisfactory performance against bacterial infection. Developing a targeting antibacterial nanoprobe combining imaging with stimulus-response antibiotic release is a promising strategy to precisely recognize lesions and enhance therapeutic efficacy for bacterial infection. In this work, we report a pH-responsive theragnostic nanoplatform for targeted imaging and local drug release at the bacterial infection site. The nanoplatform consists of the core-shell structure with persistent luminescence nanoparticles (PLNPs) as the core for autofluorescence-free luminescence imaging and zeolitic imidazolate framework-8 (ZIF-8) as the shell to act as a carrier for antibiotics cefazolin. The core-shell nanostructure is further conjugated with folic acid to facilitate the uptake and accumulation of the nanoparticles, and realize the autofluorescence-free targeted imaging of the infection site. The acidic microenvironment at the bacterial infection site enables ZIF-8 to decompose for specific drug release improve the performance in bacterial infection treatment. The developed pH-responsive nanotheranostic probe is promising for autofluorescence-free targeted imaging and therapy of bacterial infection.

Introduction

Infection triggered by pathogenic bacteria poses ever-growing threat to the worldwide human health.[1] As one of the most common pathogens, *Staphylococcus aureus* can cause various diseases including meningitis, pustulosis, conjunctivitis, mumps, etc.[2–4] Cefazolin (CEZ) is an effective drug against *Staphylococcus aureus*. It can combine with the penicillin binding protein on the bacterial cell membrane to inhibit the synthesis of bacterial cell wall and promote bacterial dissolution and death.[5,6] Direct use of antibiotics often leads to insufficient drug concentration being delivered to the target sites, resulting in poor therapeutic effects.[7,8] Controllable and targeted release of antibiotics at infected sites has shown promising prospects for improving therapeutic performance.[9,10] Future therapeutic strategies must prioritize the development of multifunctional nanomaterials for antibiotic delivery. Suitable nanocarriers can ensure drugs delivery to infected sites and sustainably drugs release for a long time, extending the time of action of drugs on lesion tissue to enhance antibacterial efficiency.[11,12]

Metal organic frameworks (MOFs), mainly consisting of metal ions/clusters and organic ligands, are emerging as attractive nano-porous materials. Due to their variable structure, adjustable pore size, excellent thermal and chemical stability, MOFs have been promoted as ideal drug carriers for controlled release of antibiotics.[13–16] As an important member of MOFs, zeolitic imidazolate framework-8 (ZIF-8) has demonstrated its potential as an ideal antibiotic carrier due to sensitive pH-response effect. ZIF-8 nanocrystals employed to carry bactericidal agents such as ciprofloxacin, gentamicin, vancomycin and other drugs exhibited good antibacterial effects for antimicrobial therapy.[17–20] The good stability in physiological environments, but rapid decomposition under weakly acidic condition make ZIF-8 promising for controlled and precise release of loaded drugs at the weak acidic infection site.[21,22]

The ideal drug treatment requires long-term retention of the drug in the lesion area and on-demand release of the drug.[23–25] Introducing imaging capabilities into drug delivery systems is crucial for monitoring drug release, indicating lesion location, and ultimately improving treatment efficiency.[26–28] Therefore, theranostics that integrates imaging agents and therapeutic drugs has become an important frontier of nanomedicine. Persistent luminescence (PL) nanoparticles (PLNPs) are special optical materials which can maintain long-lasting luminescence even after cessation of excitation.[29–31] The characteristic with in situ excitation-free can effectively eliminate excitation light-induced autofluorescence and scattering, improving the sensitivity of imaging.[32,33] In addition, the advantages of near-infrared (NIR) luminescence, LED light repetitive activation, and deep tissue penetration make PLNPs

[a] L.-Y. Wang, Dr. L.-X. Yan, Dr. X. Zhao, Dr. L.-J. Chen, Prof. X.-P. Yan
State Key Laboratory of Food Science and Resources
Jiangnan University
Wuxi 214122 (China)
E-mail: xpyan@jiangnan.edu.cn

[b] L.-Y. Wang, Dr. L.-X. Yan, Dr. X. Zhao, Dr. L.-J. Chen, Prof. X.-P. Yan
International Joint Laboratory on Food Safety
Jiangnan University
Wuxi 214122 (China)

[c] L.-Y. Wang, Dr. L.-X. Yan, Dr. X. Zhao, Dr. L.-J. Chen, Prof. X.-P. Yan
Institute of Analytical Food Safety, School of Food Science and Technology
Jiangnan University
Wuxi 214122 (China)

Supporting information for this article is available on the WWW under https://doi.org/10.1002/cnma.202300383

an ideal optical probe for long-term biological imaging and in vivo tracking.[34–36] PLNPs@ZIF-8 based theranostic nanoplatforms that integrate drug delivery vehicles with autofluorescence-free PL imaging have been constructed for tumor treatment.[37,38] However, the lack of targeting ability of nanoparticles could reduce the therapeutic effect of drugs. Therefore, it is urgent to develop nanotheranostic probes for specific targeting imaging, antibiotics delivery and infection microenvironment responsive release for bacterial infection theranostics.

Herein, we report the design and fabrication of a pH-responsive theragnostic nanoplatform for targeted imaging and local drug release at the bacterial infection site. Chromium-doped NIR PLNPs is used as the core for autofluorescence-free and NIR LED light re-activatable luminescence imaging.[39] ZIF-8 was coated on the surface of the PLNPs to obtain a core-shell structure PLNPs@ZIF-8 to provide abundant channels for subsequent antibiotic CEZ loading, and meanwhile to serve as a switch for antibiotic release in acidic environment. To further improve the antibacterial efficiency, the CEZ loaded PLNPs@ZIF-8 (PLNPs@ZIF-8-CEZ) (simplified as PZC) was surface modified with folic acid (FA) to obtain the theragnostic nanoplatform PZC-FA for targeted theranostics. On the surface of bacterial cells within the biofilm, overexpressed folate receptors can recognize FA and promote specific drug uptake.[40,41] The prepared PZC-FA theragnostic platform enables targeted PL imaging of bacterial infection and effective healing of the *S. aureus*-infected mice. The developed nanotheranostic probe shows great potential for targeted autofluorescence-free bioimaging, antibiotics delivery and infection microenvironment responsive therapy of bacterial infection.

Results and Discussion

Design and characterization of PZC-FA

The design and fabrication process of the PZC-FA nanoplatform is illustrated in Scheme 1A. Chromium-doped NIR-emitting PLNPs with reactivatable NIR luminescence is selected as the imaging unit to provide deep tissue penetration and PL imaging signals without background interference.[39] Meanwhile, porous ZIF-8 shell coating provides good drug loading ability and triggers drug release in acidic abscess site. Conjugation of folic acid on the surface of PLNPs@ZIF-8 enables the accumulation of antibiotic at the abscess site to improve antibiotic utilization and reduce damage to healthy tissues. Scheme 1B illustrates the developed multifunctional nanoplatform PZC-FA for PL targeted imaging and in vivo chemotherapy of bacterial infection. PZC-FA was injected intravenously into the mice. The overexpression of folic acid receptor at bacteria-infected sites would enhance the targeting and retention of PZC-FA, achieving PL imaging of the bacterial infected sites. At the same time, the ZIF-8 shell of PZC-FA would degrade to release the antibiotic for chemotherapy under the weakly acidic condition at the infected sites. Thus, the developed PZC-FA nanoplatform enables precise release of loaded antibiotic for the therapy of bacterial infection and meanwhile effective monitoring of the treatment process.

The core-shell structure PLNPs@ZIF-8 was prepared by a mild one pot method.[39,42] The as-prepared PLNPs@ZIF-8 was characterized by transmission electron microscopy (TEM), X-ray diffraction (XRD) spectrometry, Fourier transform infrared (FT-IR) spectroscopy, thermal gravimetric analysis (TGA) and nitrogen

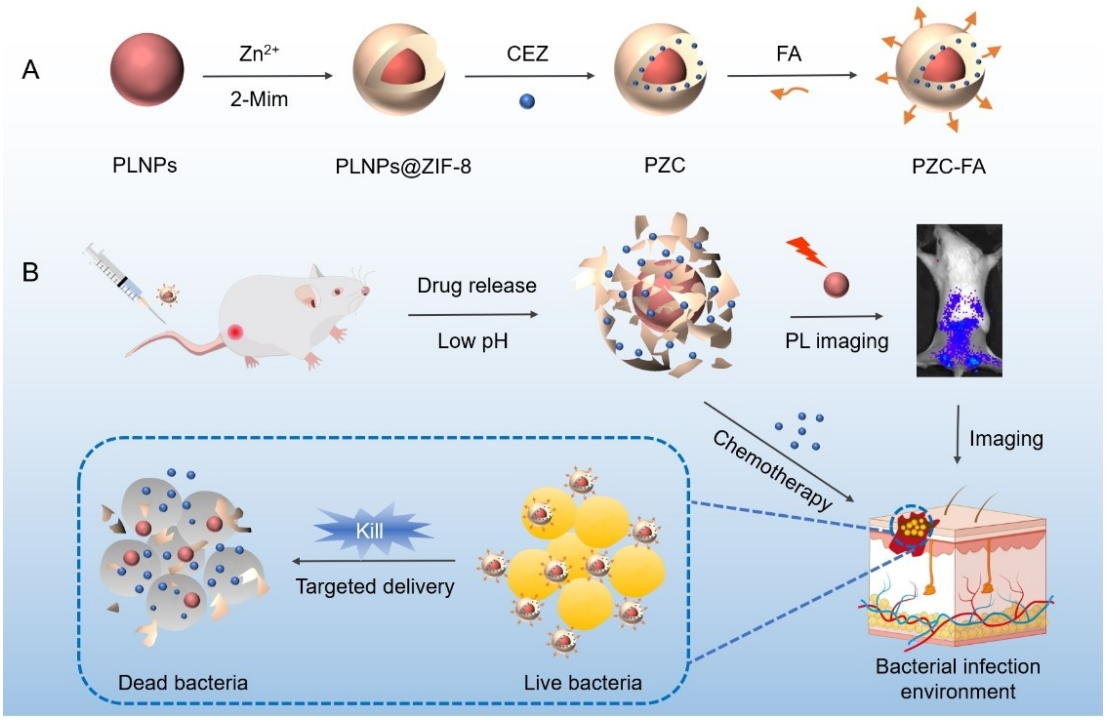

Scheme 1. Illustration for the fabrication of PZC-FA nanoplatform for the theranostics of bacterial infection.

adsorption experiment. The as-synthesized PLNPs exhibited the cube morphology with a diameter of ~14.6 nm (Figure S1) and the spinel structure of $ZnGa_2O_4$ (JCPDS 38-1240) and Zn_2GeO_4 (JCPDS 25-1018) (Figure S2). The as-prepared core-shell PLNPs@ZIF-8 gave a relatively uniform size of ca. 200 nm (Figure 1A). It also exhibited the characteristic diffraction peaks of the spinel structure of PLNPs and ZIF-8 skeleton, indicating their biphasic properties (Figure 1B). The existence of characteristic peaks for C–N bending and tensile vibrations at 995 cm^{-1} and 1145 cm^{-1}, as well as C=N stretching vibrations at 1576 cm^{-1} for ZIF-8 demonstrated the successful preparation of PLNPs@ZIF-8.[43,44] TGA curve shows a slight mass loss at 200 °C due to the removal of guest water molecules and a significant mass loss at 400 °C resulting from the decomposition of ZIF-8 (Figure 1D). The loading capacity of ZIF-8 were calculated to be 33% according to the mass loss of PLNPs@ZIF-8. The as-prepared PLNPs@ZIF-8 gave the surface area of ca. 441 m^2g^{-1} (Figure 1E), the pore volume of 0.291 $cc\,g^{-1}$ and the pore size of 0.92 nm (Figure 1F). The special micro-porous structure indicates that PLNPs@ZIF-8 would be a good drug carrier. The changes of zeta potential from −23.3 mV for PLNPs to −27.7 mV for PZC-FA (Figure S3) and hydrodynamic size from 78.82 nm (PLNPs) to the final 231.03 nm (PZC-FA) (Figure 1G) also proved the successful surface modification and drug loading. In addition, we also demonstrated the drug loading and modification process through UV-vis absorption spectroscopy (Figure 1H). After loading cefazolin, the absorption peak of cefazolin at 273 nm appeared in PZC. In addition, PZC-FA exhibited characteristic absorption peaks belonging to FA at 285 nm and 360 nm (Figure 1I).

Luminescence performance of PZC-FA

The as-synthesized PLNPs exhibited a 700 nm emission peak under 254 nm excitation (Figure S4A). The luminescence signal of the PLNPs could be easily captured and reactivated by red LED light, demonstrating the potential for long-term in vivo bioimaging (Figure S4B). The emission peak of PZC-FA is located at 700 nm, which is the same as the emission wavelength of PLNPs, indicating that it retains the NIR luminescence performance of PLNPs (Figure 2A). In addition, PZC-FA maintained a continuous luminescence signal after being irradiated under 254 nm UV light for 5 min, while the luminescence signal can be repeatedly re-activated by a red LED light (Figure 2B). The penetration depth of the nanoprobe was about 12 mm (Figure S5). All the results suggest that the obtained PZC-FA inherited the good PL imaging performance of PLNPs for bioimaging.

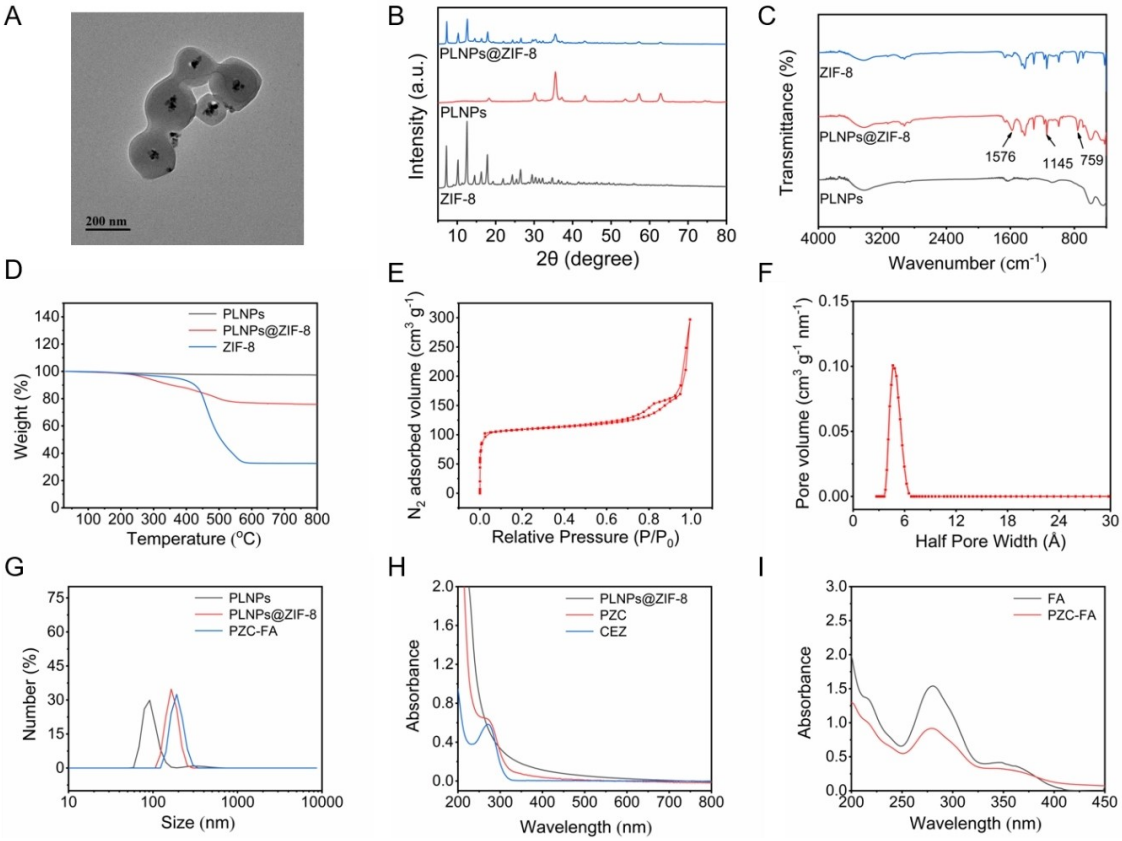

Figure 1. (A) TEM image of PLNPs@ZIF-8. (B) XRD patterns of the as-prepared PLNPs, ZIF-8, PLNPs@ZIF-8. (C) FT-IR spectra of PLNPs, ZIF-8, PLNPs@ZIF-8. (D) TGA curves of PLNPs, ZIF-8 and PLNPs@ZIF-8. (E) Nitrogen adsorption-desorption isotherm of PLNPs@ZIF-8. (F) Pore size distribution of PLNPs@ZIF-8. (G) Hydrodynamic diameter distribution of PLNPs, PLNPs@ZIF-8 and PZC-FA. (H) UV-vis absorption spectra of PLNPs@ZIF-8, PZC and CEZ. (I) UV-vis absorption spectra of PZC-FA and FA.

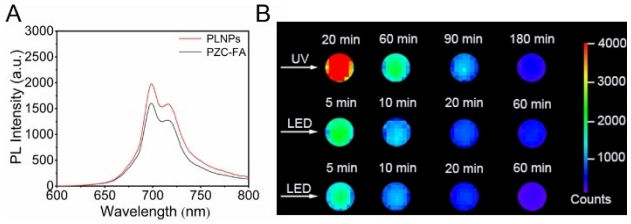

Figure 2. (A) PL intensity of PLNPs and PZC-FA. (B) PL images of PZC-FA aqueous dispersion after irradiation by a UV lamp for 5 min and re-activation with a red LED light for 2 min.

Drug release under different pH conditions

A drug loading and release experiment was further performed to explore the feasibility of PLNPs@ZIF-8 as a pH-responsive drug delivery system for treating bacterial infection. To measure the drug loading capacity of PLNPs@ZIF-8, the concentration of cefazolin in the solution before and after CEZ loading on PLNPs@ZIF-8 were measured by UV-vis absorption spectrometry. The cefazolin loading capacity was calculated to be 167.1 $\mu g\,mg^{-1}$ (Figure S6 and Figure 3A). The good drug loading capacity mainly stems from the structural characteristics of ZIF-8 due to its large specific surface area for the adsorption of cefazolin as well as the binding of the Zn^{2+} in the ZIF-8 with CEZ.

We then conducted a pH-responsive drug release study based on the absorbance of cefazolin at 273 nm. As shown in Figure 3B, CEZ released slowly in a simulated physiological environment (pH 7.4) with 27.66% of cumulative release within 24 h. This indicates that the material has a certain degree of stability under physiological conditions, which can avoid damage to the body caused by the early release of drugs during the blood circulation process. However, under weak acidity environment of simulated bacterial infection (pH 5.5), CEZ released significantly with a release amount of 58.29% of cumulative release. Acidic environment enables the break of the bonds between metal ions and organic ligands in ZIF-8 to release the loaded drugs (Figure S7).[37,38,45] This pH-response behavior allows specific and controllable release of loaded drugs at bacterial infection site to treat bacterial infection.

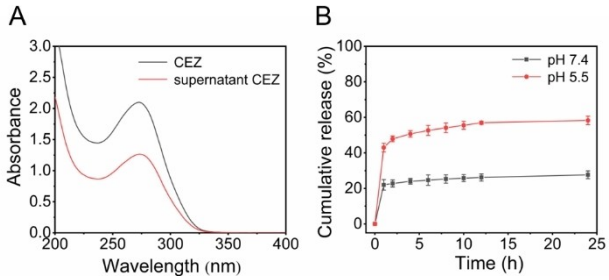

Figure 3. (A) UV-vis spectra of CEZ solution before loading and the supernatant of CEZ solution after loading. (B) Release profiles of CEZ from PZC in neutral (pH 7.4) and acidic (pH 5.5) media.

In vitro antibacterial activity

S. aureus, the most typical etiological agent of biofilm related clinical infection, was chosen as the model for antibacterial experiment. The potential antibacterial performance of PZC-FA for *S. aureus* was evaluated by the plate counting method. PZC-FA exhibited dose-dependent antibacterial ability (Figure 4A and Figure 4B). Moreover, PZC-FA shows stronger antibacterial effect at lower pH with the same concentration, indicating its pH-dependent antibacterial ability. The results are consistent with the pH-responsive behavior of PZC-FA. In addition, live/dead staining experiments were performed to reveal the bactericidal effect of PZC-FA. The living bacteria with intact cell membrane can be labeled with Calcein-AM to show green fluorescence, while the cell membrane of the damaged cells could be penetrated by propidium iodide (PI) to stain the dead bacteria red. The control group showed obvious green fluorescence but almost no red fluorescence, indicating good bacterial growth and low mortality rate. However, the bacteria in PZC-FA group shows strong red fluorescence, which proved that almost all the bacteria were killed (Figure 4C). All the above results indicate that the prepared PZC-FA composite has good antibacterial performance.

The morphology of the bacteria was further observed by scanning electron microscopy (SEM) (Figure S8). The bacterial cell structure in the control group was complete, smooth, and full. However, after co-incubation with PZC-FA, the bacterial cell structure was destroyed, resulting in the change and collapse of membrane permeability, leakage of cytoplasmic content, and bacterial death.

To study the targeting capability of PZC-FA, the bacteria were incubated with PZC-FA and observed by laser confocal scanning microscopy (LCSM). After incubating PZC-FA with *S. aureus* for 1 h, a bright red luminescence was observed on the bacterial surface from the laser confocal imaging area, proving the attachment of PZC-FA to the bacterial surface (Figure S9). The above results show the potential of PZC-FA in monitoring treatment processes and precise sterilization applications.

Cytotoxicity assay and hemolysis experiment

Nanodrug delivery systems not only require sensitive drug release response, but also have low cytotoxicity and good biocompatibility. The standard MTT method was used to examine the cytotoxicity of PLNPs@ZIF-8 to normal cells. The mouse fibroblast 3T3 cells were incubated with the cell culture medium containing different concentrations of PLNPs@ZIF-8 for 24 h. It was found that the survival ratio of the cells was maintained above 80% at 200 $\mu g\,mL^{-1}$, indicating their satisfactory biocompatibility and feasibility as drug carriers for antibacterial therapy (Figure S10). Additionally, hemolysis tests were accomplished to explore the impact of PZC-FA on red blood cells (RBCs). The hemolysis rate was below the permissible limit (5%) even at 500 $\mu g\,mL^{-1}$ PZC-FA, demonstrating the negligible damage to RBCs (Figure 4D).[46] Therefore, PZC-FA has good biocompatibility and low long-term biological toxicity,

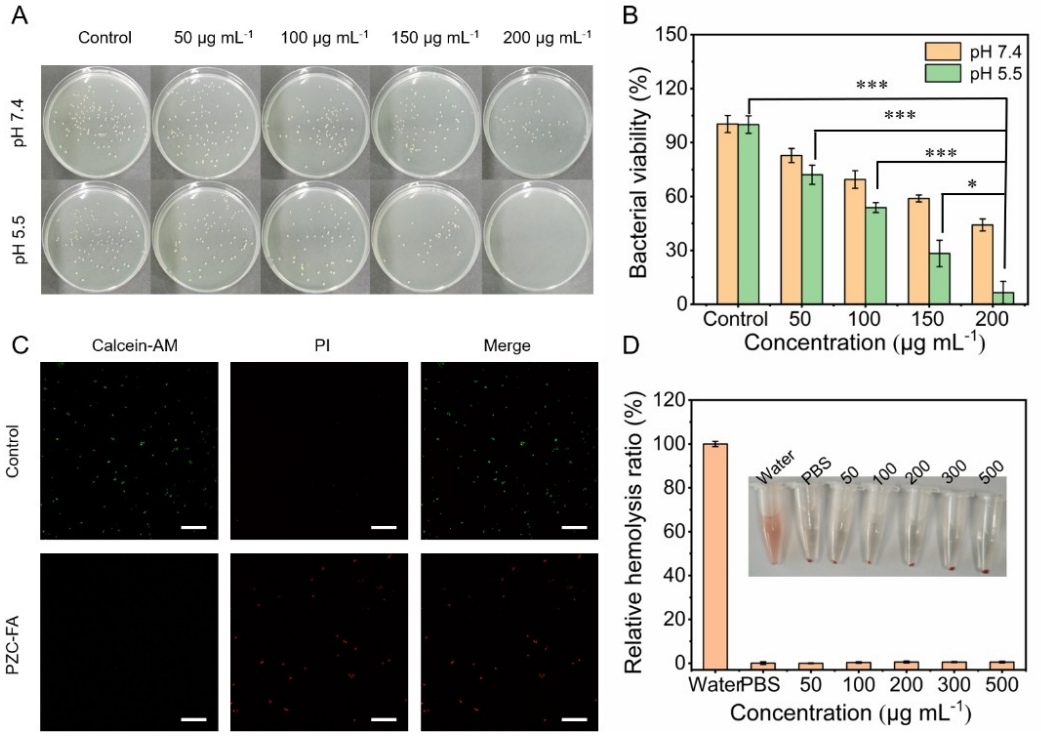

Figure 4. (A) Digital photographs of *S. aureus* bacterial colonies in the presence of different concentrations of PZC-FA at pH 5.5 and 7.4. (B) Corresponding bacterial viabilities after treatments with various concentrations of PZC-FA at pH 5.5 and 7.4. Data expressed as mean ± SD (n = 3; *P < 0.05, ***P < 0.001). (C) Fluorescent staining images of *S. aureus* with live bacteria (green) and dead bacteria (red) after various treatments (scale bar: 30 μm). (D) Hemolysis rate of red blood cells incubated with PZC-FA at various concentrations (the insert is the corresponding photograph of red blood cells with different treatment). Data expressed mean ± SD (n = 3).

making it promising alternative for in vivo antibacterial application.

Targeted PL imaging of bacterial infection in vivo

S. aureus-infected mice model were established to investigate the targeted imaging effect of PZC-FA on bacterial infection site. PZC and PZC-FA nanoparticles were injected intravenously into the mice, respectively, for comparison. At specific time points, the NIR luminescence images of mice were obtained. Before each acquisition of imaging signal, an LED red light (650 nm) was used to illuminate for 2 min. Within 24 h after injection, the luminescence signal of the material in mice was monitored (Figure 5A). In the PZC group, no visible luminescence signals were observed at the bacterial infection site at all collection time points. However, after 1 h of injection, significant luminescence signals were observed at the bacterial infection site in the PZC-FA group. The luminescence signal became increasingly apparent over time, indicating the quick targeting and continuous accumulation of PZC-FA in infected lesion. This is of great significance for monitoring the targeted chemotherapy. Besides, the relative PL intensity of isolated organs were tested (Figure 5B). As a typical reticuloendothelial system, the liver area gave major luminescence signal because of the strong phagocytosis, but other organs showed few residues.

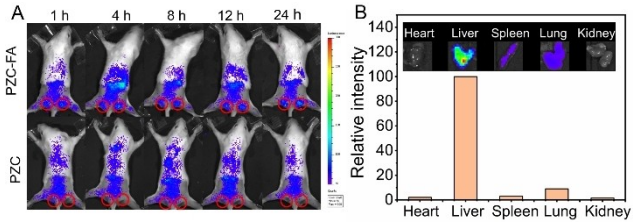

Figure 5. (A) In vivo PL imaging at various time points of *S. aureus*-infected mice intravenously injected with PZC and PZC-FA for 2 min LED excitation before each acquisition. (B) Representative PL images and luminescence of isolated organs from the mice after intravenous injection of PZC-FA for 12 days.

PZC-FA for in vivo treatment of *S. aureus*-infected mice

In view of the remarkable biocompatibility and antibacterial activity of PZC-FA in vitro, we further established subcutaneous abscess animal model to explore the therapeutic efficacy. The mice with *S. aureus* infection were randomly divided into four groups: PBS, PLNPs@ZIF-8, PZC, and PZC-FA. The PZC-FA group showed significantly better recovery of abscess site at the same time point among all the groups within 12 days treatment (Figure 6A). The abscess at the infected site disappeared, scabs peeled off, and the skin became smooth in the PZC-FA group, while significant scabs were observed in the other three groups. In addition, the PZC-FA group had faster abscess healing speed (Figure S11). To further verify the therapeutic effectiveness, the

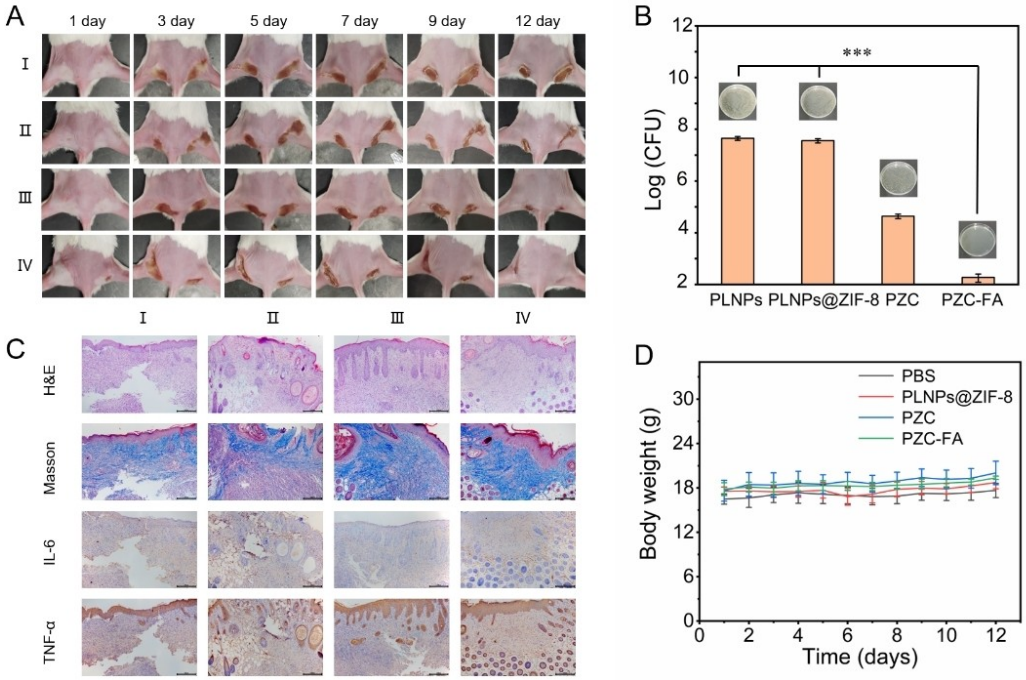

Figure 6. (A) Photographs of the *S. aureus*-infected abscesses of the mice in different treatments, (I) PBS, (II) PLNPs@ZIF-8, (III) PZC, (IV) PZC-FA. (B) The corresponding LB plate photographs and bacterial counts from infected tissues with different treatments. Data expressed mean ± SD (n = 3; ***P < 0.001). (C) H&E, Masson's trichrome staining and immunofluorescence staining of IL-6 and TNF-α images of infected tissues from different treatments, (I) PBS, (II) PLNPs@ZIF-8, (III) PZC, (IV) PZC-FA (scale bar: 200 μm). (D) Body weight changes of mice from different treatments. Data expressed mean ± SD (n = 5).

skin tissue at the abscess site were counted using the plate counting method after 12 days. As shown in Figure 6B, the PZC-FA group gave markedly fewer bacterial colonies than the other three groups, suggesting the capability of PZC-FA for the effective treatment of bacterial infection. On the fifth day after the end of the treatment, no recurrence of infection was found at the wound site (Figure S12).

The skin tissues of mice were collected after treatment for hematoxylin and eosin (H&E), Masson's trichrome staining and immunohistochemical staining to check the inflammation and healing degree of the infected wounds. The results are shown in Figure 6C. The PBS group exhibited massive inflammatory cells infiltrating the wound, while the PZC-FA treatment group from showed a relatively complete epidermal structure, newly formed hair follicles and blood vessels in the abscess tissue. During the wound healing process, collagen is synthesized and serves as the backbone for new tissue growth.[47] Therefore, the amount of collagen can also be used as an indicator to evaluate the effectiveness of wound healing. Masson staining showed that the collagen fibers in the wound tissue of PZC-FA were dense and orderly, indicating better wound repair. The pro-inflammation cytokines TNF-α and IL-6 in infected abscesses were evaluated through immunohistochemistry staining as typical inflammatory cytokines are involved in the formation of inflammation, leading to immune dysfunction and hindering tissue recovery. The IL-6 and TNF-α values of the PZC-FA treatment group were significantly reduced, indicating that this composite material reduced inflammation and accelerated the healing of infected wounds. During the entire treatment process, the mice did not experience any deaths and their weight steadily increased (Figure 6D). Also, the H&E staining results show no obvious histopathological abnormalities in the major organs (liver, spleen, heart, lung, and kidney) (Figure S13). All the above results confirm that the side effects of PZC-FA in vivo is negligible. Therefore, PZC-FA is a promising antibacterial agent against bacterial infection.

Conclusions

We have reported a multifunctional nanoplatform PZC-FA for autofluorescence-free targeted PL imaging and pH-responsive antibiotic therapy of bacterial infection. The developed PZC-FA nanotheranostic probe integrates the autofluorescence-free and renewable NIR PL imaging of PLNPs, the good drug loading and pH-responsive drug release of porous material ZIF-8 as well as the good targetability of FA to bacteria-infected site. PZC-FA has been successfully applied to in vivo treatment of *S. aureus*-infected mice. This nanoplatform can not only improve drug utilization, but also reduce side effects on normal tissue, being promising for the treatment and monitoring of bacterial infection.

Experimental Section

Synthesis of PLNPs and PLNPs@ZIF-8

The PLNPs was prepared according to Zhao et al.[39] Core-shell PLNPs@ZIF-8 was prepared based on previously reported literatures.[42] The PLNPs solution (1 mL, 2.5 mg mL^{-1}) was added to a methanol solution of 2-methylimidazole (10 mL, 10 mM) and the solution was sonicated for 15 min. Subsequently, the $Zn(NO_3)_2 \cdot 6H_2O$ (10 mL, 10 mM) methanol solution was added into the mixed solution, and reacted at room temperature for 2 h. The product was separated by centrifugation (10000 rpm, 10 min), washed with methanol three times, and dried overnight under vacuum at 60 °C.

Loading of cefazolin

20 mg of PLNPs@ZIF-8 were uniformly dispersed in 20 mL of methanol solution containing cefazolin (500 μg mL^{-1}). This suspension was kept stirring at room temperature for 24 h. After reaction, the resulting PLNPs@ZIF-8-CEZ (PZC) was collected by centrifugation and washed with methanol to remove the adsorbed drug on the surface. The powder product was dried at 60 °C under vacuum.

Preparation of PZC-FA

The obtained PZC nanoparticles were dispersed into a 2 mg mL^{-1} FA solution and stirred at room temperature for 12 h to produce PZC-FA nanocomposites. Finally, the product was separated by centrifugation and washed with deionized water.

pH-responsive drug release

The pH-responsive drug release behavior was carried out by dispersing PZC in PBS solution. In short, PZC (1 mg mL^{-1}) nanoparticles were suspended in 8 mL of PBS (pH 7.4 and pH 5.5, separately). These suspensions were kept shaking at 150 rpm at 37 °C. At different time intervals, the suspensions were centrifuged at 10000 rpm for 10 min.1 mL of the supernatant was collected and immediately replaced by an equal volume of fresh PBS to maintain solution equilibrium. The amount of released CEZ was determined via UV-vis spectrophotometry. The cumulative release percentage of CEZ (CR%) was calculated using the following formula: $CR\% = M_r/M_t \times 100\%$, where M_r is the amount of released CEZ and M_t is the total amount of loaded CEZ.

Antibacterial experiments in vitro

The antibacterial ability of PZC-FA against *S. aureus* (Gram-positive bacteria) was evaluated using the plate counting method. Bacteria were cultured in 5 mL of liquid culture medium in a constant temperature shaker (37 °C, 200 rpm) for 12 h. The cultured bacterial solution was centrifuged and resuspended in the LB (pH 5.5) to 10^8 CFU mL^{-1} for further antibacterial testing. 100 μL bacterial suspension was mixed with different concentrations of PZC-FA (0, 50, 100, 150, 200 μg mL^{-1}) for 12 h. Then, 100 μL of diluted bacterial suspensions from each group were cultured on agar plates at 37 °C for 18 h to count the bacterial colonies.

Animal model

All animal procedures were approved by the Animal Ethics Committee of Jiangnan University (JN. No 20230415b0200608). The experimental female BALB/c mice (5-6 weeks old) were purchased from Changzhou Cavens Laboratory Animal Co., Ltd. (Changzhou, China). A subcutaneous abscess model was constructed to appraise the PL imaging ability and antibacterial efficacy of PZC-FA. Firstly, 100 μL of *S. aureus* (10^8 CFU mL^{-1}) was subcutaneously inoculated in the rear back of the mice. After 24 h, subcutaneous abscess was formed in each mouse.

In vivo PL imaging

PZC and PZC-FA (200 μL, 4 mg mL^{-1}) were respectively injected intravenously into the *S. aureus*-infected mice to investigate the targeted imaging ability. The luminescence images on the IVIS imaging system at different time points (1 h, 4 h, 8 h, 12 h, and 24 h) were obtained and used to observe the distribution of the material in vivo. Before each imaging, the mice were irradiated with a 650 nm LED light for 2 min.

In vivo antibacterial activity

The *S. aureus*-infected mice were randomly divided into four groups (n = 5). The mice were treated with PBS, PLNPs@ZIF-8, PZC and PZC-FA (200 μL, 4 mg mL^{-1}) by intravenous injection. The wound area and body weight of different treated mice were recorded every day. The Image J software was used to quantitatively calculate the changes in wound area. After 12 days, all mice were sacrificed, and the related wound tissues and main organs were excised. All of them were fixed in 4% paraformaldehyde for histological analysis. The bacterial suspensions of the skin tissues were used to evaluate the wound infection recovery by the plate counting method.

Acknowledgements

This work was supported by the National Natural Science Foundation of China (No. 21934002), and the Collaborative Innovation Center of Food Safety and Quality Control in Jiangsu Province.

Conflict of Interests

The authors declare no conflict of interest.

Data Availability Statement

The data that support the findings of this study are available in the supplementary material of this article.

Keywords: Drug delivery · Persistent luminescence · Antibacterial · Nanotheranostics · Bioimaging

[1] Z. L. Xue, X. L. Li, Y. B. Li, M. Y. Jiang, G. Z. Ren, H. R. Liu, S. J. Zeng, J. H. Hao, *Nanoscale.* **2017**, *9*, 7276–7283.
[2] M. Zhang, H. R. Zhang, J. Feng, Y. L. Zhou, B. L. Wang, *Chem. Eng. J.* **2020**, *393*, 124778.
[3] S. Juneja, J. Bhattacharya, *Colloids Surf. B.* **2019**, *182*, 110349.
[4] A. J. Huh, Y. J. Kwon, *J. Controlled Release* **2011**, *156*, 128–145.
[5] I. K. Yazdi, M. B. Murphy, C. Loo, X. W. Liu, M. Ferrari, B. K. Weiner, E. Tasciotti, *J. Tissue. Eng.* **2014**, *5*, 2041731414536573.

[6] A. Dastneshan, S. Rahiminezhad, M. N. Mezajin, H. N. Jevinani, I. Akbarzadeh, M. Abdihaji, R. Qahremani, M. Jahanbakhshi, Z. A. Lalami, H. Heydari, H. Noorbazargan, E. Mostafavi, *Chem. Eng. J.* **2023**, *455*, 140544.
[7] M. S. Tonetti, F. D'Aiuto, L. Nibali, A. Donald, C. Storry, M. Parkar, J. Suvan, A. D. Hingorani, P. Vallance, J. Deanfield, *J. Vasc. Surg.* **2007**, *45*, 1286–1287.
[8] F. Graziani, D. Karapetsa, B. Alonso, D. Herrera, *Periodontol. 2000.* **2017**, *75*, 152–188.
[9] F. Nazir, T. A. Tabish, F. Tariq, S. Iftikhar, R. Wasim, G. Shahnaz, *Drug Discovery Today* **2022**, *27*, 1698–1705.
[10] C. Wang, Y. Yang, Y. Y. Cao, K. X. Liu, H. Shi, X. D. Guo, W. Y. Liu, R. Z. Hao, H. B. Song, R. T. Zhao, *Biomater. Sci.* **2023**, *11*, 432–444.
[11] Y. Suzuki, M. Tanihara, Y. Nishimura, K. Suzuki, Y. Kakimaru, Y. Shimizu, *J. Biomed. Mater. Res.* **1998**, *42*, 112–116.
[12] A. Nazli, D. L. He, D. D. Liao, M. Z. I. Khan, C. Huang, Y. He, *Adv. Drug Delivery Rev.* **2022**, *189*, 114502.
[13] K. D. Lu, T. Aung, N. N. Guo, R. Weichselbaum, W. B. Lin, *Adv. Mater.* **2018**, *30*, 1707634.
[14] A. L. Feng, Y. N. Wang, J. Z. Ding, R. Xu, X. D. Li, *Curr. Drug Delivery* **2021**, *18*, 297–311.
[15] Y. J. Sun, L. W. Zheng, Y. Yang, X. Qian, T. Fu, X. W. Li, Z. Y. Yang, H. Yan, C. Cui, W. H. Tan, *Nano-Micro Lett.* **2020**, *12*, 103.
[16] M. X. Wu, Y. W. Yang, *Adv. Mater.* **2017**, *29*, 103.
[17] V. C. Ramos, C. B. Garcia Reyes, G. M. Garcia, M. I. S. Quesada, F. J. Martinez-Checa Barrero, J. J. S. Rabago, M. S. Polo, *Pharmaceutica* **2022**, *14*, 2546.
[18] J. Yang, C. L. Liu, Y. N. Ding, T. C. Sun, X. H. Bai, Z. K. Cao, S. Ramakrishna, J. Zhang, Y. Z. Long, *Int. J. Biol. Macromol.* **2021**, *189*, 698–704.
[19] Y. Y. Liu, Z. H. Li, S. Y. Zou, C. B. Lu, Y. Xiao, H. Bai, X. L. Zhang, H. B. Mu, X. Y. Zhang, J. Y. Duan, *Int. J. Biol. Macromol.* **2020**, *155*, 103–109.
[20] W. Zhang, Y. N. Zhou, Y. T. Fan, R. Cao, Y. Y. Xu, Z. Z. Weng, J. Ye, C. He, Y. Zhu, X. L. Wang, *Adv. Mater.* **2022**, *34*, 2105738.
[21] D. F. S. Gallis, K. S. Butler, J. O. Agola, C. J. Pearce, A. A. McBride, *ACS Appl. Mater. Interfaces.* **2019**, *11*, 7782–7791.
[22] Z. T. Liu, Y. Z. Yi, S. J. Wang, H. X. Dou, Y. Fan, L. M. Tian, J. Zhao, L. Q. Ren, *ACS Nano.* **2022**, *16*, 16549–16562.
[23] D. Liu, F. Yang, F. Xiong, N. Gu, *Theranostics.* **2016**, *6*, 1306–1323.
[24] X. L. Lu, R. H. Chen, J. Lv, W. C. Xu a, H. J. Chen, Z. B. Ma, S. S. Huang, S. Li, H. Liu, J. Hu, L. M. Nie, *Acta Biomater.* **2019**, *99*, 363–372.
[25] Z. J Fan, Y. C. Wang, L. Q. Li, F. C. Zeng, Q. P. Shang, Y. H. Liao, C. H. Liang, Liming Nie, *ACS Nano.* **2022**, *16*, 16177–16190.
[26] J. X. Wang, C. J. Yao, B. Shen, X. H. Zhu, Y. Li, L. Y. Shi, Y. Zhang, J. L. Liu, Y. L. Wang, L. N. Sun, *Theranostics.* **2019**, *9*, 608–619.
[27] J. M. Xiao, G. L. Zhang, R. Xu, H. Chen, H. J. Wang, G. Tian, B. Wang, C. Yang, G. Bai, Z. Y. Zhang, H. Y. Yang, K. Zhong, D. H. Zou, Z. Y. Wu, *Biomaterials.* **2019**, *216*, 119254.
[28] D. H. Liu, Z. J. Zhou, X. Y. Wang, H. Z. Deng, L. Sun, H. X. Lin, F. Kang, Y. Zhang, Z. T. Wang, W. J. Yang, L. Rao, K. K. Yang, G. C. Yu, J. S. Du, Z. Y. Shen, X. Y. Chen, *Biomaterials.* **2020**, *244*, 119979.
[29] S. K. Sun, H. F. Wang, X. P. Yan, *Acc. Chem. Res.* **2018**, *51*, 1131–1143.
[30] K. Huang, N. Le, J. S. Wang, L. Huang, L. Zeng, W. C. Xu, Z. J. Li, Y. Li, G. Han, *Adv. Mater.* **2022**, *34*, 2107962.
[31] L. L. Liang, J. Y. Chen, K. Shao, X. Qin, Z. F. Pan, X. G. Liu, *Nat. Mater.* **2023**, *22*, 289–304.
[32] Z. W. Pan, Y. Y. Lu, F. Liu, *Nat. Mater.* **2012**, *11*, 58–63.
[33] L. J. Chen, S. K. Sun, Y. Wang, C. X. Yang, S. Q. Wu, X. P. Yan, *ACS Appl. Mater. Interfaces.* **2016**, *8*, 32667–32674.
[34] A. Abdukayum, J. T. Chen, Q. Zhao, X. P. Yan, *J. Am. Chem. Soc.* **2013**, *135*, 14125–14133.
[35] Y. J. Li, X. P. Yan, *Nanoscale.* **2016**, *8*, 14965–14970.
[36] J. L. Kong, R. Zou, G. L. Law, Y. Wang, *Sci. Adv.* **2022**, *8*, eabm7077.
[37] H. X. Zhao, G. Shu, J. Y. Zhu, Y. Y. Fu, Z. Gu, D. Y. Yang, *Biomaterials* **2019**, *217*, 119332.
[38] Y. Lv, D. D. Ding, Y. X. Zhuang, Y. S. Feng, J. P. Shi, H. W. Zhang, T. L. Zhou, H. M. Chen, R. J. Xie, *ACS Appl. Mater. Interfaces.* **2019**, *11*, 1907–1916.
[39] X. Zhao, K. C. Zhao, L. J. Chen, Y. S. Liu, J. L. Liu, X. P. Yan, *Chem. Sci.* **2021**, *12*, 442–452.
[40] M. Z. Yu, G. K. Zhang, P. L. Li, H. J. Lu, W. T. Tang, X. Yang, R. B. Huang, F. Yu, W. Z. Wu, Y. H. Xiao, X. D. Xing, *Mat. Sci. Eng. C.* **2021**, *127*, 112225.
[41] X. Chen, Y. N. Liu, A. G. Lin, N. Huang, L. Q. Long, Y. Gang, J. Liu, *Biomater. Sci.* **2018**, *6*, 1923–1935.
[42] M. Zeng, Z. G. Chai, X. Deng, Q. Li, S. Q. Feng, J. Wang, D. S. Xu, *Nano Res.* **2016**, *9*, 2729–2734.
[43] J. F. Yao, R. Z. Chen, K. Wang, H. T. Wang, *Microporous Mesoporous Mater.* **2013**, *165*, 200–204.
[44] A. F. A. Latip, M. Z. Hussein, J. Stanslas, C. C. Wong, R. Adnan, *Chem. Cent. J.* **2013**, *7*, 119.
[45] H. Y. Zhang, Q. Li, R. L. Liu, X. K. Zhang, Z. H. Li, Y. X. Luan, *Adv. Funct. Mater.* **2018**, *28*, 10.
[46] P. Liu, Y. R. Wang, L. An, Q. W. Tian, J. M. Lin, S. P. Yang, *ACS Appl. Mater. Interfaces.* **2018**, *10*, 38833–38844.
[47] X. Q. Yu, J. Zhao, D. D. Fan, *Chem. Eng. J.* **2022**, *437*, 135475.

Manuscript received: August 9, 2023
Revised manuscript received: September 30, 2023
Accepted manuscript online: October 7, 2023
Version of record online: October 24, 2023